Modeling of Aqueous Poly(oxyethylene) Solutions. 2. Mesoscale Simulations

Jan Fischer,[†] Dietmar Paschek,[‡] Alfons Geiger,[‡] and Gabriele Sadowski*[,†]

Laboratory of Thermodynamics and Department of Physical Chemistry, Dortmund University of Technology, 44221 Dortmund, Germany

Received: July 1, 2008; Revised Manuscript Received: August 20, 2008

We extend our work on aqueous solutions of poly(oxyethylene) oligomers $H-(CH_2-O-CH_2)_n-H$ (POE_n). On the basis of atomistic simulations of trimer and decamer solutions (first part of this series of papers), different sets of coarse-grained implicit-solvent potentials have been constructed using the iterative Boltzmann inversion technique. The comparison of structures obtained from coarse-grained simulations (gyration radii, end-to-end distances, radial distribution functions) with atomistic reference simulations and experiments shows that the state-specific potentials are transferable both to a wide concentration range, if the same molecule size is considered, and to at least 2 orders of magnitude larger molecules (in terms of molecular mass). Comparing the performance of different mesoscale potentials, we find different applicability ranges in terms of molecule sizes. The experimental gyration radii for chains comprising up to 1500 monomers are reproduced almost quantitatively by the decamer-fitted potentials with dihedral interactions included. The trimer-fitted potentials reproduce experimental chain dimensions of up to some hundred monomers but seem to become metastable beyond a certain chain length, as we evidenced some chain collapses. Relaxation of large-scale features is 1−2 orders of magnitude faster in the mesoscale simulations than in the atomistic simulations. The diffusion behavior in dependence of concentration is captured correctly when the decamer potential is applied to the decamer itself. For all other chain lengths, we find that time mapping from coarse-grained to atomistic trajectories has to be determined separately for each concentration. Overall, diffusion is 1−2 orders of magnitude faster on the mesoscale, depending considerably on the Lowe−Andersen thermostat parameters. The CG simulations provide an overall speed-up of about 3 orders of magnitude.

1. Introduction

Although computer power is increasing at high speed, standard atomistic molecular simulation techniques still suffer from severe limitations of both accessible time and length scales. This is especially relevant in the area of macromolecules such as polymers, or biomolecules. Accordingly, efforts to circumvent these limitations based on coarse-graining the atomistic model onto a mesoscale one have recently been increased.[1−6] Common to different coarse-graining approaches is that a reduced number of interaction centers in combination with "softer" or flattened-out potentials[7] as well as accelerated dynamics lead to significant speed-ups, extending affordable system sizes and physical times. Structural approaches aim at finding the effective potential that reproduces the structural properties of a specific underlying atomistically detailed system (either from simulation or experiment), motivated by Henderson's theorem that states that the knowledge of the particle densities and all pair correlations in a liquid uniquely fixes the multibody Hamiltonian of the system.[8]Recently, this has been verified numerically for three popular spherically symmetrical pair potentials.[9] Some closely related methods for structural coarse-graining exist, consisting essentially of an iterative sequence of mesoscale simulations with (a) trial potential(s) corrected in each step. The iteration finally leads to the convergence of the actual structure toward its target function. The potential correction step may consist of a simplex[3,4] optimization, of the solution of a set of linear equations involving the actual and target function(s) (inverse Monte Carlo)[10] or of the application of a term that involves the ratio of actual and target function to determine the potential correction numerically (reverse Monte Carlo and Boltzmann inversion).[11−13] Apart from these, there are different methods, e.g., based on the solution of the Ornstein−Zernike equation[14−16] or a force-matching method recently proposed by Izvekov and Voth.[17] In this work, we apply the so-called iterative Boltzmann inversion method.[12,13] This technique has successfully been applied to polymer melts[18,19] and solutions[1,4,12,13] as well as to low-molecular species.[14,20] It is conceptually simple, allows any type and number of distribution function as input, and converges relatively fast. Here, we focus on its application to aqueous solutions of poly(oxyethylene) and its oligomers as a test case, thereby extending our atomistic modeling work[21,22] to the mesoscale. The scope of this work is to explore the capability of the coarse-grained potentials derived at one specific state point in describing structure at both different concentrations and for longer polymer chains and to compare the static and dynamical properties of potentials that were fitted to different molecular sizes. Transferability to longer chains of coarse-grained potentials fitted to small analogues has successfully been demonstrated for some cases,[4,18] but focus was either on melts or very diluted solutions and only limited attempts were made to explore transferability in solutions, both to larger molecule size and different concentrations. We are aware of two coarse-grained potentials for POE, an *analytical* coarse-grained model[23] fitted to a melt of POE_{30} and an implicit-solvent numerical coarse-grained model for aqueous POE solutions,[5] which was presented recently and used in simulations of poly(oxyethylene)−poly(oxypropylene) triblock copolymer micelles in water. The

* Corresponding author. E-mail: g.sadowski@bci.tu-dortmund.de. Phone: +49-(231)-755-2635. Fax: +49-(231)-755-2075.
† Laboratory of Thermodynamics.
‡ Department of Physical Chemistry.

10.1021/jp805770q CCC: $40.75
Published on Web 10/08/2008

TABLE 1: Simulation Details of Atomistic Reference Simulations and Mesoscopic Simulations That Were Used to Fit the Respective Coarse-Grained Potentials

	n_{POE}	n_{water}	box (nm)	T (K)	P (bar)	ρ (kg m^{-3})	simulated time (ns)
Trimer Potential Set							
atomistic reference	128	1036	3.91	298	1.0	1006.4 ± 5	14 ns
mesoscopic fit	128		3.91	298	(NVT)	484	1−10 ns per iteration step
Decamer (Both Potential Sets)							
atomistic reference	16	418	2.84	298	1.0	1058.9 ± 8	60 ns
mesoscopic fit	16		2.84	298	(NVT)	484	1−10 ns per iteration step

authors made no systematic effort to validate its transferability to longer chains.

The outline of the paper is as follows: After presenting simulation details of the mesoscale simulation techniques we used, we shortly discuss our implementation of the iterative Boltzmann inversion. In the results section, we first compare the different sets of coarse-grained potentials we fitted. We then explore the trimer potential transferability in terms of both concentration and molecule size by comparison of atomistic and mesoscale simulation results, before we continue with an assessment of the applicability of three different potential sets to polymer solutions of considerably higher molar mass, including a short discussion of relaxation features on both scales. Finally, we examine in brief the influence of the thermostat on diffusion and the time mapping from the mesoscale back to the atomistic scale.

2. Methods

2.1. Atomistic Simulations. The methods used for atomistic simulations were decribed in the first part of this publication.[21,22] All results that served for comparison with mesoscale simulations were generated using the TIP4P-Ew water model[24] and the TraPPE-UA with modified dihedral parameters[21] (see first part of this series of publications). Some details of the atomistic reference simulations are summed up in Table 1.

2.2. Mesoscale Simulations. The simulations of the coarse-grained systems were performed using a modified version of the MD code MOSCITO[25] that uses numerical potentials for all types of inter- and intramolecular interactions: nonbonded, bond stretches, bond bending, and dihedrals. The potentials and forces are tabulated in equidistant intervals of distances or angles. Forces and potentials are interpolated using the Newton−Gregory interpolation scheme, and equations of motions are integrated applying the Leap-frog algorithm. All simulations were performed in the NVT ensemble at 298 K using an orthorhombic box employing periodic boundary conditions. No electrostatics is present in the mesoscale simulations. A cutoff of 1 nm was applied for all mesoscale simulations. Cutoff corrections were obsolete, because all tabulated potentials were forced to have zero values at distances larger than the cutoff. A Verlet-type neighbor list for the nonbonded interactions was applied, constructed by a linked-cell algorithm[26] with a neighbor list cutoff 1 Å larger than the nonbonded interactions cutoff. The temperature was imposed by a Lowe−Andersen thermostat,[27] which used a second list of neighboring pairs within the thermostat cutoff. Both lists were updated automatically depending on the displacement of the particles. Time steps ranged from 1 to 5 fs.

Lowe−Andersen Thermostat. This thermostat was originally proposed as an alternative to dissipative particle dynamics but is suitable for MD simulations as well. It is similar to the Andersen thermostat[28] that also assigns random velocities drawn from a Maxwell−Boltzmann distribution, but the Lowe-Andersen thermostat works on the component of the *relative velocity* parallel to the line of centers of the particles, instead of working on absolute velocities. It is applied after each integration step of the equation of motion. There are two thermostat parameters to fix: the thermostat radius R_T and the "bath collision probability" $\Gamma\, dt$. Only pairs of particles within this distance R_T of each other are considered for possible collisions, while the bath collision probability $\Gamma\, dt$ (between 0 and 1, where 1 corresponds to colliding every particle in every step) decides about the actual collision itself. Within the algorithm, all pairs of particles within R_T are considered sequentially and the postcollisional new relative velocity is drawn from a Maxwellian distribution corresponding to the desired temperature. For details of the implementation, see the papers by Lowe et al.[27,29] We consider it ideally suited for implicit-solvent mesoscale simulations, because it samples the canonical ensemble, it ensures good temperature control up to very big time steps, and it additionally mimics the effect of collisions between solute molecules and the omitted solvent particles. Thus, it maintains liquidlike hydrodynamic conditions at particle densities that refer to a gaslike state. The viscosity of the "solution" depends on the thermostat parameters and increases drastically with increasing collision radius and collision frequency. This additional friction effect should therefore be minimized. The time-step dependence of temperature or equilibrium properties is negligible,[29,30] and a slow-down of diffusion as encountered with the Andersen thermostat can be prevented in small-molecule systems by the use of low thermostatting rates, as shown by Koopman and Lowe.[29] It turns out, however, that diffusion in the polymer systems considered here is affected very much by the collision frequency (see below). Two different strategies can be applied to fix the thermostat parameters. One approach, recently proposed by Lowe and Koopman,[29] aims at minimizing the collision radius while the collision probability is 1. This corresponds to a rather realistic picture where neighboring particles are collided each time they get very close to each other. This radius is in principle easy to find for potentials with well-defined hard sphere radii like Lennard-Jones potentials. It is however not obvious how to fix such a minimal collision radius in simulations with oscillatory potential, and for low-density systems, this may result in too small collision numbers as molecule encounters get scarce, corresponding to gaslike conditions. We therefore adopted a second, more pragmatic approach: we set the collision radius to a higher value and sought the appropriate low number of collisions necessary for acceptable temperature control. R_T was generally set to be equal or greater than the nonbonded potential cutoff radius (10−20 Å). For good temperature control, collision frequencies had to be between approximately three to five collisions per femtosecond.

2.3. Constructing Coarse-Grained Potentials by Iterative Boltzmann Inversion. We constructed our set of potentials by applying the so-called iterative Boltzmann inversion (IBI) method of Müller-Plathe et al.[13] The method essentially consists of three steps: (a) performing an atomistic simulation to create the particles' trajectories from which target function(s) can be

extracted afterward; (b) choosing how to group together atoms from the detailed level onto the mesoscale level (i.e., mapping) and extraction of the coarse-grained topologies and target functions; (c) performing the actual iteration by repeatedly simulating the system in its mesoscale representation and evaluating the functions of interest. After each iteration loop, the potential(s) 1,..., n are corrected according to the formula

$$U^j_{i+1}(x) = U^j_i(x) + RT \ln \frac{P^j_i(x)}{P^j_{\mathrm{tgt}}(x)} \qquad j = 1,...,n \quad (1)$$

$P^j_{\mathrm{tgt}}(x)$ denotes the target distribution for the jth potential, $P^j_i(x)$ denotes the jth distribution function resulting after iteration loop i and from the use of the actual potential $U^j_i(x)$. $P^j(x)$ has to be replaced by the appropriate distribution function of the independent coordinate x, either a distance or an angle. Each distribution function $P^j(x)$ is uniquely associated to one potential $U^j(x)$. Nonbonded potentials between specific sites A−B are associated with the corresponding radial distribution function $g_{\mathrm{A-B}}(r)$. Bond, angle, or dihedral potentials are accordingly associated with the appropriate bond length, bond-bending angle, or dihedral angle distribution functions $P(l)$, $P(\varphi_{ijk})$, or $P(\varphi_{ijkl})$, respectively. The iteration is stopped when an appropriate convergence criterion is met. The potentials resulting from this procedure are tabulated. To start the iteration cycle, one has to specify a starting potential. In principle, the choice is arbitrary, but an obvious choice is either a simple Lennard-Jones potential or the potential of mean force (PMF). For the different potential types, the PMF can directly be calculated from the target functions as

$$U_{\mathrm{PMF,nb}}(r) = RT \ln g_{\mathrm{tgt}}(r) \quad (2)$$

for nonbonded, bond-bending, bond-stretching, and dihedral

$$U_{\mathrm{PMF,ang}}(\varphi) = RT \ln \frac{P_{\mathrm{tgt}}(\varphi)}{\sin \varphi} \quad (3)$$

$$U_{\mathrm{PMF,bd}}(r) = RT \ln P_{\mathrm{tgt}}(r) \quad (4)$$

$$U_{\mathrm{PMF,dihed}}(\varphi) = RT \ln P_{\mathrm{tgt}}(\varphi) \quad (5)$$

interaction potentials, respectively.[12,13]

As described by Reith,[12] it is useful to start with a potential as short-ranged as possible to accelerate iteration. Hence, for the nonbonded potential, we used a truncated potential of mean force after its attractive short-ranged part. We thus used the inherent information of the target distribution and kept the starting potential as short-ranged as possible at the same time. For bond, angle, and dihedral potentials, the potentials as calculated by eqs 3−5 were used. First, the exclusively intramolecular potentials for bonds and bends were iterated, before we turned to the nonbonded potential. All distribution functions and potentials were smoothed by simple running averages of 3−7 points. To ensure that both nonbonded potentials and forces vanish to zero at the cutoff, we multiplied the force and the potential with a hyperbolic tangent tapering function that smoothly approaches zero. Each iteration step consisted of several equilibration runs until the total energy and the pressure of the system did not deviate more than 1% from their running averages and subsequent production runs of typically some nanoseconds. We required that the total energy, the pressure, and the distribution functions of interest be converged before continuing with the next potential correction. Energy and pressure evaluated from subsequent runs did not differ more than 1% and the structural distribution functions evaluated and averaged from evenly spaced parts of the trajectories had typical average relative deviations of less than 1%.

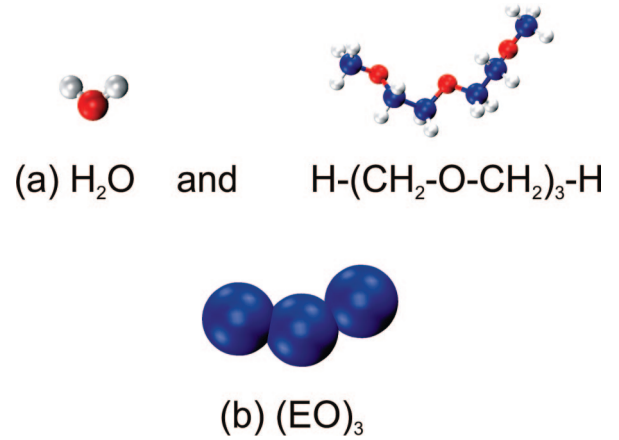

Figure 1. Applied mapping scheme for poly(oxyethylene) water solutions. The atomistic representation (a) is mapped onto its coarse-grained implicit-solvent counterpart (b) by assigning the mesoscale group "EO" to the center of mass of each [$H_2C-O-CH_2$] repeat unit ([$H_3C-O-CH_2$] unit at molecule ends).

3. Results and Discussion

3.1. Mesoscale Models for Aqueous Poly(oxyethylene) Solutions. To derive a coarse-grained potential for poly(oxyethylene), we first had to choose the mapping scheme. To preserve enough detail of each chemical moiety, we decided to apply a rather low level of coarsening, mapping the repeat unit $-CH_2-O-CH_2-$ containing three united atoms onto one coarse-grained "EO" site. Several studies suggest that using rather small degrees of coarsening leads to better potential transferability to temperature[19,20,31] or chain length.[11] Other choices would have been possible, e.g., taking each glycol unit $-CH_2-CH_2-O-$ as a new center. However, taking this "EO" site seemed the most natural choice, as it preserves symmetry and it results in only one type of nonbonded interaction with a not too complicated radial distribution function. Chain end sites were treated as being identical in interaction but having a different mass due to the three hydrogens. To derive the target functions, atomistic coordinates were mapped onto coarse-grained ones by taking the center of mass of each repeat unit (see Figure 1). The smallest POE oligomer with all intramolecular interactions present on the *atomistic scale* is dimethoxyethane (DME). In the coarse-grained picture, using the mentioned mapping scheme, the smallest molecule with all intramolecular interactions present is the tetramer. To keep things simple first, as it was not known a priori if a dihedral interaction is necessary for longer molecules, we first took the trimer $H[-CH_2-O-CH_2]_3-H$ as a starting point for the potential iteration, because it incorporates bonds and bends.

Potentials Based on the Trimer. The distance, bond, and angle distributions between the EO coordinates at the intermediate concentration $x_{\mathrm{POE3}} = 0.11$ were taken as target functions. Details of the atomistic and mesoscale simulation can be found in Table 1. The intramolecular bond-stretching and bond-bending potentials model interactions between two and three

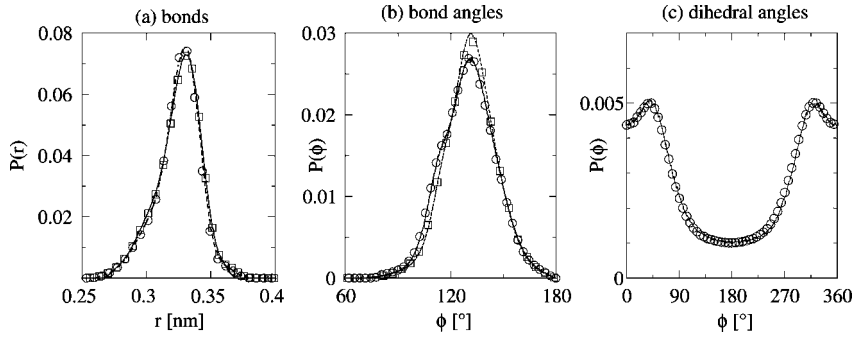

Figure 2. Histograms of intramolecular degrees of freedom between the monomers for the poly(ethyleneoxide) trimer and decamer in water at $w_{POE} = 0.48$. The symbols denote the target distributions extracted from atomistic simulations using the modified TraPPE-UA force field;[21] the lines show the final trial distributions from Boltzmann iteration using coarse-grained molecular dynamics simulations. (a) Bond distance distribution between two neighboring EO sites (squares, trimer; circles, decamer). (b) Angle distribution between three joint EO sites (squares, trimer; circles, decamer) site. (c) Dihedral angle distribution between four joint EO sites (circles, decamer potential fit).

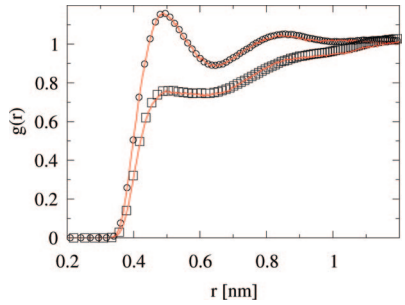

Figure 3. Intermolecular radial distribution functions between mesoscale ethylene oxide (EO) units in aqueous solution. The lines denote final radial distribution functions from Boltzmann iteration potential fits (lines for decamer fits with and without dihedrals are virtually indistinguishable). Circles correspond to the target function for POE_3 and squares to the target function for POE_{10}. Both at $w_{POE} = 0.48$ ($\rho_{POE} = 484$ kg/m^3). Both targets are from atomistic trajectories at 298 K and 1 bar. Mapping as depicted in Figure 1.

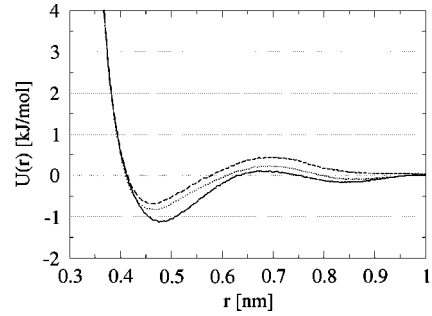

Figure 4. Final nonbonded potentials between mesoscale interaction sites "EO" from Boltzmann iteration (cutoff 1 nm). Full line, POE_3 fit; broken line, POE_{10} fit without dihedral potential; dotted line, POE_{10} fit using an additional dihedral potential. Both at $w_{POE3} = 0.48$ ($\rho_{POE} = 484$ kg/m^3). Mesoscale sites were mapped as described in Figure 1.

sequential EO sites, respectively, while the nonbonded potential only describes *inter*molecular interactions. Within simulations of longer molecules (see section 3.3), the same potential was also used to describe *intra*molecular nonbonded interactions between sites separated by more than two bonds. In order to get the set of potentials, we proceeded as described by Reith et al.[13] and fitted the different potential contributions in the order of their (assumed) relative strengths:

$$U_{stretch} \rightarrow U_{bend} \rightarrow U_{nonbonded}$$

The underlying assumption is that the intramolecular, bonded interactions can be considered relatively independent from the nonbonded ones. The bond length distribution for EO−EO quickly converged to the target value after a few iterations. The angle distribution of three successive EO sites could also be reproduced very well after only a few iterations. Then, we turned to the nonbonded potential between EO sites. Starting with the potential of mean force, truncated after the first minimum, the target function was reproduced almost perfectly after approximately 10 iterations. Because of slight deviations in the bond and angle distributions, we repeated the iteration of all three potentials in the same order for some steps. The resulting angle and bond length histograms are shown in Figure 2, and the radial distribution target function together with the final result from iteration is shown in Figure 3. The match is very good, with the largest deviation of $g(r)$ being less than 0.01 at every distance and less than 1% for the bond or angle distribution. Deviations become larger beyond the potential cutoff but are still below 1%. The corresponding intermolecular EO−EO nonbonded potential is shown in Figure 4 (full line). The structure of the potential is complex, showing a primary minimum around 4.8 Å, a small very weakly repulsive region and a second very shallow minimum at larger separations. As the choice of cutoff for the mesoscale potentials is in principle arbitrary, we simply kept the atomistic cutoff. A longer cutoff might have been necessary if the target distribution function had included more long-scale features, because only features of the distribution function within the cutoff influence the potentials via eq 1. A comparison of Figures 3 and 4 shows that, for the trimer, the maxima and minima of the radial distribution function (rdf) roughly correspond to minima and maxima in the potential.

Potentials based on the Decamer. We constructed two other sets of potentials based on target functions from the *decamer*. The first set consists of three potentials (bonds, bends, nonbonded) and *does not incorporate an explicit dihedral interaction*; the 1−4 interactions are simply modeled using the nonbonded potential. The second set of decamer potentials *does incorporate dihedral interactions* to describe 1−4 interactions. We decided to parametrize a dihedral potential, because simulations with the 1−4 interactions modeled by the nonbonded potential produced a rather flat dihedral angle distribution with slightly more trans than gauche conformations (compare Figure 6, upper panel), while in atomistic simulations, the EO units take on mainly gauche conformations (compare Figures 2c and 6, lower panel). Both decamer potentials were fitted to target distributions extracted from atomistic simulations at the same mass density of POE as the trimer potentials, $\rho =$

484 kg/m^3 (molar concentration $x_{POE10} = 0.037$). Simulation details can be found in Table 1.

Both bond length and angle distributions are rather similar for the trimer and decamer (compare Figure 2). Each coarse-grained angle comprises six connected atomistic dihedrals and hence represents the average conformations of these dihedrals. The angle distributions being similar reflect the similarity of the underlying atomistic conformations of triads of EO units in either the trimer or decamer. Nevertheless, to include the subtle differences, we refitted all potentials for the decamer in the same order as described above for the trimer. The POE_{10} potential of mean force is completely repulsive, which makes it difficult to use it as a starting point for the iteration: a very repulsive region leads to near-zero values of the trial $g(r)$ at small distances, which in turn makes the potential correction in this region ill-defined. Therefore, we started again with the short-ranged PMF of POE_3. Both bond and angle distributions converged within two to four iteration cycles. After fitting the nonbonded potential, we repeated the consecutive fitting in the order bond → angle → nonbonded (→ dihedral) potential, because the fit of intramolecular distributions had slightly worsened. For the second decamer potential set, the above-mentioned sequence was repeated using the first set of decamer potentials. We used the dihedral PMF (eq 5) as a first guess for the dihedral potential. The target dihedral angle distribution and the final fitting result are depicted in Figure 2c. The final set of potentials could simultaneously represent the bond, angle, and dihedral distributions (Figure 2) and the radial distribution function (Figure 3) of the decamer very well. All *nonbonded* potentials for both the decamer and trimer are presented in Figure 4.

The decamer potentials are similar to the POE_3 potential but show some important differences: a less attractive first minimum at short distances, shifted to smaller distances, and a completely repulsive region (potential without dihedral interactions) for distances greater than approximately 6 Å. This reflects the differences found in the $g(r)$ of the decamer and trimer (compare Figure 3). The decamer rdf indicates that there are less close contacts among the monomers than in the trimer solution. This effect is modeled in the decamer potentials via the more repulsive midrange region. Although the nearest neighbor minimum corresponds to the first maximum in the target function like in the trimer potential, the structure at longer distance shows no easily interpretable one-to-one correspondence any more. Both our trimer and decamer potentials resemble the 12-mer potential of Bedrov et al.,[5] which was also obtained by iterative Boltzmann inversion. Their potential is very similar to our decamer potential which incorporates the 1−4 dihedral interactions, as both include a slightly attractive tail again at larger distances. Their target functions were extracted from atomistic simulations of POE_{12} chains in TIP4P water at $w = 0.52$ ($x = 0.035$). Our decamer target function (Figure 3) looks rather similar to their 12-mer target function. The minor differences in the potentials could be attributed to differences between the target distributions as well as to minor differences in the iteration procedure. The deviations among the mesoscopic distributions can be traced back to differences between the underlying atomistic force field. They produce different conformer populations, as shown by us in the first part of this series of papers.[21,22]

3.2. Applicability of the Trimer Potentials to Different Concentrations. The trimer potential was fitted at one specific state point, namely 298 K, 1 bar, and $x_{POE3} = 0.11$. It is often assumed that there is a very limited transferability in concentration for mesoscale potentials. To examine to what extent the radial distribution functions at both higher and lower concentrations could be reproduced, we compared distribution functions from mesoscale simulations with their corresponding atomistic counterparts. Before comparison, the atomistic trajectories have been mapped onto the coarse-grained representation by assigning the actual center-of-mass positions of each [CH_2−O−CH_2] group to the "EO" sites for each frame and distribution functions have been calculated afterward. Figure 5 shows radial distribution functions from both CG simulations and atomistic simulations at varying molar POE_3 concentrations between 0.05 and 0.36 (mass concentrations 0.15−0.81). For the CG simulations, we used the average volume and the molecule numbers from the atomistic simulations to represent the respective concentration. The CG potential reproduces the structure in terms of the $g(r)$ between ethylene oxide sites at different concentrations rather well. Close to the fit concentration ($w = 0.48$), the local structure is reproduced very faithfully, and the same is true in the more concentrated system $w = 0.81$. Additional test simulations at lower concentrations indicated that, for $w \leq 0.09$, the mesoscale potential leads to more pronounced deviations from the atomistic structure with too high first and second maxima (not shown), which could be explained by a clustering of the molecules. This clustering probably indicates that transferability to very diluted systems is smaller than to more concentrated solutions. The results suggest that the CG potential transferability is greater than commonly assumed. This is, however, obviously very much dependent on the mixture under

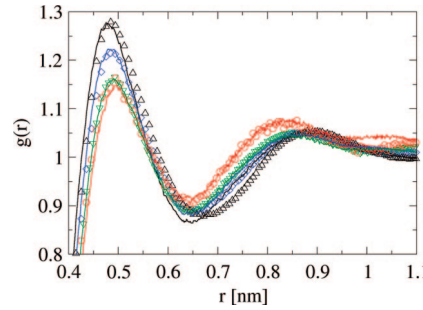

Figure 5. Radial distribution functions at different concentrations between EO sites from atomistic and coarse-grained simulations of POE_3 in water using the potentials (see Figure 4) adjusted to reproduce the structure at 298 K, 1 bar, and $w_{POE3} = 0.48$. Symbols denote results from atomistic simulations, and lines display results from mesoscale simulations. Concentrations: $w_{POE3} = 0.15$ (red)/0.48 (green)/0.66 (blue)/0.81 (black).

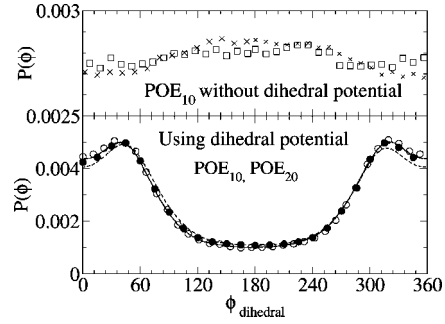

Figure 6. Distribution of dihedral angles from atomistic and mesoscale simulations ($\rho_{POE} = 484$ kg/m^3) with 1−4 interactions modeled either using the nonbonded potentials or using a dihedral potential (fitted to atomistic decamer simulation at $\rho_{POE} = 484$ kg/m^3). Upper panel: POE_{10} simulations using the trimer potentials (stars) and the decamer potentials (squares), both without dihedral potential. Lower panel: results from CG simulations of POE_{10} (open circles) and POE_{20} (filled circles) compared to distributions from atomistic simulations (full line, POE_{10}; broken line, POE_{20}).

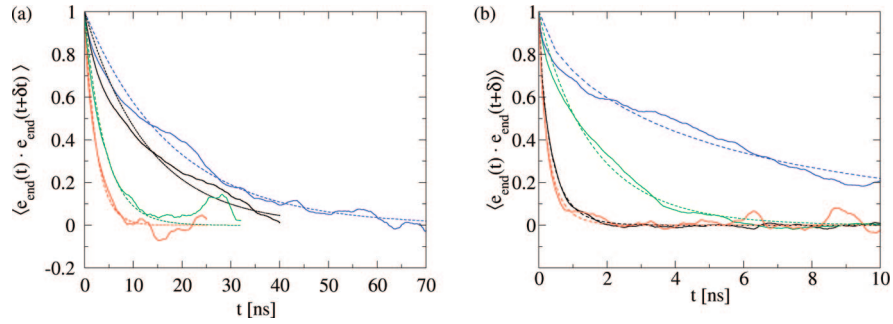

Figure 7. Orientational autocorrelation function of unit vectors parallel to the vectors connecting the chain ends from (a) atomistic and (b) mesoscale simulations (trimer potentials) of poly(oxyethylene) in water for different polymer chain lengths at 298 K. Full lines denote simulation results; broken lines are exponential fits (a) and stretched exponential fits (b) of the curves. (a) Number of monomers are 10 (red), 12 (green), 20 (black), and 30 (blue). (b) Number of monomers are 10 (red), 20 (black), 30 (green), and 100 (blue). Lowe thermostat bath collision frequency of 5 fs^{-1} and thermostat radius of 10 Å. All simulations at a POE density of $\rho_{POE} = 484$ kg/m^3, except for the 100-mer at $\rho_{POE} = 240$ kg/m^3.

consideration, on the adequacy of the chosen mapping scheme, and on the chosen reference state to which the potentials are fitted. Silbermann et al.[14] compared implicit-solvent potentials generated from different concentrations of ethanol in water and found that the potentials were very concentration-dependent. An explanation for our good transferability may be that we preserve more of the identity of chemical groups, while Silbermann et al. mapped entire molecules onto one coarse-grained site. Transferability can only be expected if the molecules can rearrange their local structure, which is impossible if all internal degrees of freedom are omitted. A limited concentration transferability was also observed by Reith for PVA in hexane.[12]

3.3. Transferability of Mesoscale Potentials to Longer Chain Molecules. ***Dense Structures.*** In order to further explore the transferability of both sets of mesoscale potentials in terms of molecule size, the same long-chain systems we had simulated in atomistic detail before[21] were now simulated using the mesoscale representation for direct comparison. We conducted NVT simulations at 298 K using the average box sizes of the atomistic NPT simulations and arbitrarily chosen snapshots from the atomistic simulations' trajectories, which were mapped onto the mesoscale representation and subsequently taken as starting structures. Additionally, simulations of longer chains with $n =$ 40, 100, and 200 without atomistic reference data were performed for comparison with experimental data. As there were no atomistic reference simulations, the structures could not be extracted the same way as in the simulations for 3−30 monomers; we chose to fix the POE mass density at 484 kg/m^3 for comparison, which is the same as in the atomistic reference simulation of the trimer (molar concentration $x = 0.11$). These long-chain structures were generated by (a) construction of several separate single-chain structures in elongated conformations, (b) short equilibration runs for the isolated chains, and (c) combination of several single-molecule structures from different simulations into one box. The box size was adjusted to the desired monomer density afterward. In some cases, this procedure had to be repeated until an appropriate structure with not too many overlaps was found. Alternatively, to reach a feasible starting point for simulation of these dense structures, and as decorrelation and dynamics was very slow for the high-density structures (mass density of POE alone $\rho_{POE} \approx 484$ kg/m^3 refers to a higher "real" density because of the left-out waters, see next section), we first carried out simulations at half the POE density $\rho_{POE} \approx 240$ kg/m^3 and took snapshots from these simulations with adjusted boxes to start simulations of the denser systems.

Relaxation of Large-Scale Features. In order to both evaluate the speed-up of relaxation features compared to atomistic simulations and check if the long-scale features we wanted to compare could be decorrelated within simulation, we calculated the end-to-end-vector autocorrelation functions for the coarse-grained simulations. Figure 7 shows results for simulations with the trimer potential set (all POE mass densities at 484 kg/m^3 identical to atomistic reference simulations, except for 100-mer at 240 kg/m^3) and for the atomistic simulations. The CG simulation curves could be fitted to (stretched) exponential functions given by

$$P(t) = \exp(-(t/\tau_{end})^{\beta}) \qquad (6)$$

τ_{end} denotes the autocorrelation time and β the stretching exponent. The smaller oligomers' decorrelation curves could be fitted to purely exponential functions, while, for 30 and more monomers, a stretched exponential was more appropriate. Decorrelation of the end-to-end-vectors of the 100- and 200-mers at the higher density of 484 kg/m^3 was not complete after 250 ns, which prompted us to simulate at half the density as well. At 240 kg/m^3, the 100-mer could be decorrelated when a low collision rate (5 fs^{-1}) was employed (compare Figure 7), which was still not the case for the 200-mer. Figure 8 shows results using the two sets of *decamer* potentials for 100-mer (lower panel) and 200-mer (upper panel). The curves with the same thermostat parameters ($\Gamma = 5$ fs^{-1}, $R_{th} = 1$ nm) in Figures 7 and 8 can directly be compared. First, we note that the decorrelation is significantly slower for the decamer set *without* dihedral interactions (full symbols) than for the set that incorporates those interactions (open symbols). As the dihedral potential favors gauche-like conformations (compare Figure 6) where the beads approach closer, this may lead to more frequent close contacts and corresponding higher forces and acceleration.. The 200-mer now can also be completely decorrelated, while it stays trapped in its initial state for a long time when using the trimer potentials. Second, we note that these comparisons are only valid for the same set of thermostat parameters, since increasing thermostat collisions slow down reorientation very much. This is exemplified by the curves for the 100-mer using either 5 or 10 collisions per femtosecond in Figure 8. On the other hand, the collisions have to be above a certain threshold (mostly 2−5 fs^{-1}) for sufficient temperature control.

In order to compare the relaxation behavior of the various simulations, the correlation time τ_{cor} has been calculated by integrating the autocorrelation function $P(t)$ over time:

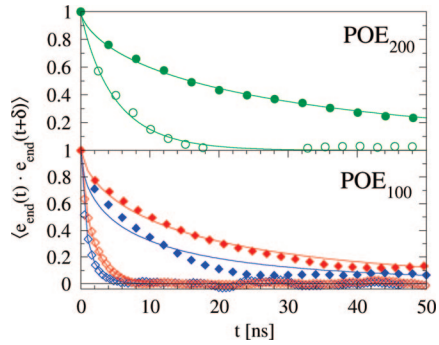

Figure 8. Orientational autocorrelation function of end-to-end vectors from *implicit-solvent* mesoscale simulations of poly(oxyethylene) in water for oligomers of 100 and 200 monomers. Simulations at 298 K and $\rho_{POE} = 240$ kg/m^3 employing the decamer-fitted potentials and using a thermostat radius of $R_T = 1$ nm. Full symbols, decamer potentials without dihedral interactions; open symbols, decamer potentials including dihedral interactions. Lower panel: 100-mer, collision frequency of $\Gamma = 5$ fs^{-1} (blue symbols) or $\Gamma = 10$ fs^{-1} (red symbols). Upper panel: 200-mer, $\Gamma = 5$ fs^{-1}. Lines are stretched exponential fits to the data.

$$\tau_{cor} = \int_0^\infty P(t)\, dt \qquad (7)$$

τ_{cor} is identical to τ_{end} for the exponential decay. Figure 9 shows a compilation of characteristic correlation times evaluated from eq 7 for the atomistic as well as different CG simulations. The data have been regressed by power fits, with exponents as indicated in the caption. The correlation times for atomistic simulations[21,22] are at least 1 order of magnitude larger for all monomer numbers than those from CG simulations. Among the coarse-grained potential sets, the decamer potential with dihedral potential permits the fastest relaxation, followed by the decamer potential without dihedrals and the trimer potential. The latter two behave very similarly. The dependency on chain length is less pronounced for the CG potentials than in atomistic simulations ($\sim n^{1.85}$). This means that the larger the molecules, the more advantageous is the use of the CG potentials compared to atomistic simulations, since the factor τ_{at}/τ_{CG} will grow with growing chain length.

Comparison with Atomistic and Experimental Data. Figure 10a shows a comparison of chain dimensions in terms of the radii of gyration and end-to-end distances from coarse-grained simulations with the three sets of potentials compared to the corresponding atomistic simulation data. The error associated with the radii of gyration and end-to-end distances from the mesoscopic simulations is approximately 0.3 and 0.7 nm, respectively. In order to make a proper comparison between atomistic and mesoscopic simulations, we first mapped the atomistic trajectory coordinates onto the corresponding EO sites as described above. Then, these pseudomesoscopic trajectories were evaluated. The absolute differences between atomistic radii of gyration directly evaluated from the unaltered atomistic trajectories and those calculated after mapping are small (order of magnitude 1 Å), but not accounting for this would lead to significant relative deviations of approximately 25% for the trimer and still 3% for the 30-mer, decreasing with molecule length. The "original" values from atomistic simulations *without mapping* are greater, because on average the atomistic sites are further apart than the centers of the corresponding "EO" group. As Figure 10 demonstrates, the gyration radii from atomistic simulations are very well reproduced for 3−30 monomers by the trimer potentials at the examined (relatively concentrated) state points. An origin of the slight overestimation of the end-to-end distances might be the missing dihedral interactions (instead, the 1−4 interactions are modeled using the nonbonded potential). Comparing with atomistic gyration radii for 10−30 monomers, both sets of decamer potentials perform comparably well. The deviation for the end-to-end distance is larger without the dihedral potential. While the distribution functions of angles and distances are all in good agreement with their atomistic references, the dihedral distribution for both the decamer

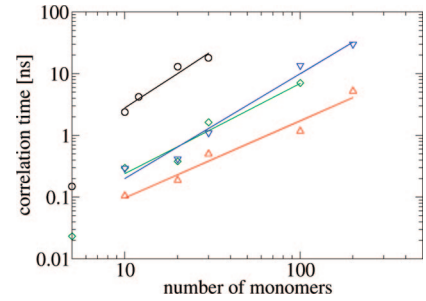

Figure 9. End-to-end-vector correlation times (eq 7) in dependence of monomer numbers for poly(oxyethylene) in water. Circles, atomistic simulations; green diamonds, CG simulations with trimer potential; blue triangles down, CG simulations with decamer potential without dihedrals; red triangles up, CG simulations with decamer potential including a dihedral potential. Simulations at 298 K and $\rho_{POE} = 484$ kg/m^3 (240 kg/m^3 for CG simulations with $n > 20$) using a thermostat radius of $R_T = 1$ nm and collision frequency of 5 fs^{-1}. Lines show regression curves $\tau_{cor} \sim n^p$ for $n \geq 10$, with $p = 1.85/1.46/1.69/1.25$ (atomistic/trimer/decamer/decamer potentials with dihedrals).

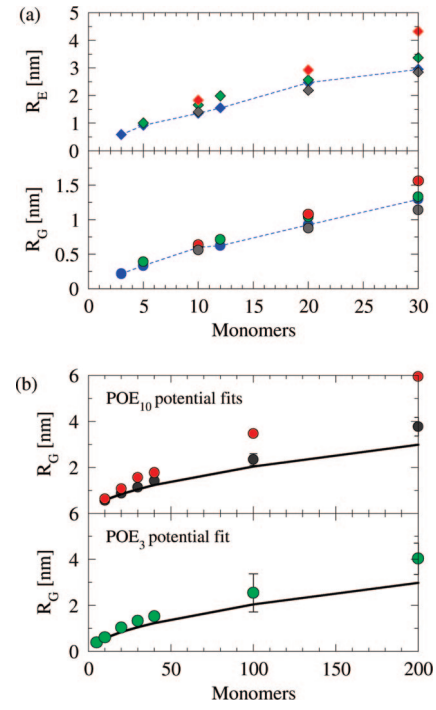

Figure 10. Dependence of radius of gyration R_G (circles) and end-to-end distance R_E (diamonds) on chain length for poly(oxyethylene) in water at 298 K and 1 bar. (a) R_G and R_E from *atomistic simulations* (blue symbols with line) compared to coarse-grained simulations with implicit-solvent potentials, employing trimer-fitted potentials (green symbols) and decamer-fitted potentials without dihedral interactions (red symbols) and decamer-fitted potentials including dihedral interactions (gray symbols). (b) R_G from coarse-grained simulations compared to values calculated by extrapolation of experimental data[32] (line). The key to the symbols is the same as in part a. All simulations and potential fits at a POE mass density of $\rho_{POE} = 484$ kg/m^3, except for 100-mer and 200-mer simulations (240 kg/m^3). Each monomer consists of one repeat unit CH_2-O-CH_2.

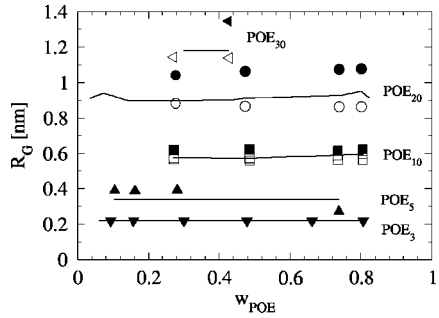

Figure 11. Concentration dependency of radius of gyration of POE_n with $n = 3$, 5, 10, 12, 20, and 30 repeat units. Atomistic simulations (lines) compared to simulations with trimer-fitted potentials (full symbols) and simulations with decamer-fitted potentials including dihedral interactions (open symbols).

potential without explicit dihedral interaction and for the trimer potentials is not (compare Figure 6). The wrong dihedral distribution leads to too extended structures with too many trans configurations. That is the reason why the decamer potential without dihedral interactions leads to too large chain structures. Both R_G and R_E of the decamer itself are reproduced perfectly by the decamer potential fit including dihedrals, but R_E is overestimated by both the trimer and the decamer potentials without dihedrals. All presented radii of gyration and end-to-end distances were evaluated from the trajectories after equilibration and after total reorientation of the end-to-end vectors, leading to 70−600 ns of simulation for the 100-mer and 200-mer. The respective converged values of different simulation runs, employing different thermostat parameters and/or different starting structures differed by up to 20% for the 100/200-mer. Hence, these values might be subject to a larger error because of less very slow convergence. We omitted the results of the higher density structures in Figure 10, because they did not depart very much from their initial values within simulations. Because of this slow decorrelation observed at the dense structures, transferability of the potentials to still bigger molecules could only be tested by simulation of isolated chains (for detailed analysis, see below).

Simultaneous Concentration and Chain Length Extrapolation. We have already shown continued applicability of the coarse-grained trimer potentials (for $g(r)$) within a limited concentration range, keeping the chain length at the same value as in the fit (section 3.2), and for a change in chain length, keeping the (monomer) concentration constant or at half the original value (last section). A third way of testing the potential applicability is to apply a simultaneous change in both (monomer) concentration and chain length. Figure 11 shows radii of gyration from atomistic and mesoscopic simulations using the trimer potentials and from simulations using the decamer-fitted potentials including dihedral potential versus mass concentration POE_3 to POE_{30}. The dependency on concentration is very weak for all examined polymer lengths. The mesoscopic potentials work very well over the examined concentration range (which translates into a density range in the implicit-solvent description) between 10 and 80 mass percent of polymer; i.e., the absolute values of radii of gyration are well reproduced, and the potentials do not show any artifacts like chain collapse. The decamer potentials can reproduce the gyration radii of 10-mer and 20-mer more closely than the trimer potentials. This is far more than what would be expected from a state-dependent implicit-solvent potential, where a certain (fixed) amount of solvent molecules per polymer molecule is implicitly present.

Single-Chain Simulations. As the examinations of relaxation behavior have shown, molecular dynamics simulations of still longer chains than presented above (>200) are only feasible for low-density structures or isolated chains. Hence, to explore further the validity of the potentials, we complemented our analysis with single-molecule simulations for polymer chains between 100 and 1500 monomers (442.3−66050 g/mol). Simulations were performed for 100−500 ns of CG time at a time step of 5 fs and collision frequencies between 5 and 20 fs^{-1}, using thermostat radii between 1 and 2 nm. Starting structures were either elongated chains or random coils, generated using the equilibrium angles and bond lengths of the atomistic model. These results can directly be compared to experimental data by Kawaguchi et al.[32] covering the range from 6000 to 1.1×10^7 g/mol. All chain lengths could be decorrelated within 10−50 ns of simulation using the decamer potentials and within similar times for the trimer potentials. However, as equilibration of chain dimensions was in general slower than reorientation, convergence had to be determined separately by inspection of the temporal evolution of gyration radii. Figure 12 shows a compilation of radius of gyration data from atomistic and coarse-grained simulations using the trimer potentials (a) and the two sets of decamer potentials (b) along with experimental data from three different sources. The estimated error associated with the reported values from block averaging of individual runs is ±0.66 nm for the end-to-end distance and ±0.18 nm for the radius of gyration for the 1500-mer; the estimated relative error for all chains is around ±1.8%. The error estimate from combining several independent simulation runs is about 5−10% for the decamer potentials. The values for the 100-mer and 200-mer in Figure 12b have a larger scatter, because they include results from both denser systems and single chains. The scatter in the trimer potential results (Figure 12a) for more than 200 monomers is considerably larger. However, taking all results from different (3−10) individual runs together, the experimental values are within the error bars (with exception of the 400-mer). This scatter is the result of an artifact occurring in simulation: the chains either showed a chain collapse into a dense structure, or they stayed fluctuating around a solvated state with a gyration radius close to the experimental one. Starting from an elongated configuration, the chains either collapsed to the more dense structure or remained in the solvated more extended structure. The collapsed structure was mostly approached rather gradually, and fluctuations were smaller in these structures. As the equilibration took very long in some cases (up to 120 ns for the 1500-mer), it might not always have been completed. The different outcomes of individual simulations are probably due to subtle differences in the preparation of starting structures as well as in the collision numbers the chains underwent. We could not find any systematic dependence on the thermostat parameters for the chain dimensions. Once the structure was collapsed, the chains stayed in this dense conformation using the trimer potentials. When taking this structure and simulating it using the decamer potentials, the solvated chain dimension was retained. The bimodal distribution of gyration radii has some similarity with a phase change, and this artifact could indicate some kind of metastability of the trimer potentials for more than 200 monomers. Similar structural artifacts were observed upon attempting the transfer of Boltzmann iterated potentials of a small glass-former to a temperature far below the state point they were fitted at.[20] For POE, it is plausible that the excluded volume effect of solvent molecules or neighboring monomers is captured better by the decamer potentials, both with and without explicit consideration of 1−4 interactions, because of its more repulsive character at intermediate distances (cf. Figure 4). This repulsive region is far

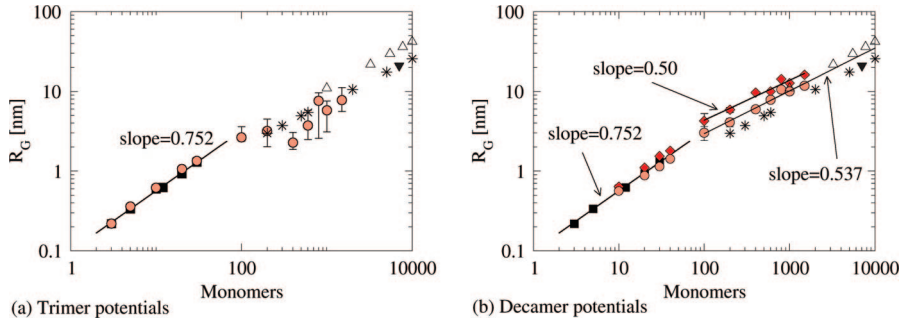

Figure 12. Radius of gyration R_G for poly(oxyethylene) in water at 298 K and 1 bar. Results from atomistic simulations (squares), experimental data for dilute concentrations and $M_w > 6000$ g/mol (stars,[32] triangles down,[39] triangles up[40] [30 °C]) and coarse-grained molecular dynamics simulations. (a) Employing the trimer-derived potentials (circles, error bars indicate the range of values from minimum to maximum) and (b) employing the decamer-derived potentials without dihedral interactions (diamonds) or with dihedral interactions (circles). Error bars mostly within symbol size. Compilation of data from isolated chain simulations (100−1500 monomers, collision frequency of 5 fs^{-1}) and simulations at ρ_{POE} = 484 or 240 kg/m^3 (3−200 monomers). Error bars for less than 100 monomers are smaller than symbol size. The lines are least-squares fits to the atomistic simulation (N = 3,..., 30) with exponent 0.752 and to the CG simulation with decamer-derived potentials for N = 200,..., 1500, with scaling exponents of 0.537 and 0.50 (with and without dihedrals, respectively).

less pronounced in the trimer potential and seems to be compensated by the second minimum. To corroborate this assumption, additional simulations were performed with a manually modified version of the trimer potential, truncated at about 0.75 nm. This potential always led to chain conformations *without collapse*, approaching the experimental values even for the 600-mer. Hence, the double-well feature might be the origin of this metastability. In not too diluted systems, its attractive character is outweighed by more excluded volume interactions and neighbor collisions. Further support for this explanation comes from our finding that the chain collapse does not occur in simulations of the 400-mer with four molecules instead of one molecule. The reproduction of experimental data for chain lengths between 200 and 1500 monomers is satisfactory for the decamer potential without dihedral interactions. The incorporation of dihedral interactions improves the agreement. Fitting the CG simulation results of 100−1500 monomers gives a scaling law of R_G (nm) = $0.065216M_W^{0.50}$ for the decamer potential without dihedrals and of R_G (nm) = $0.032556M_W^{0.537}$ with dihedral interactions included. The latter compares favorably with the reported scaling law of R_G (nm) = $0.0202M_W^{0.55}$ from ref 32. The 10-mer potential set with dihedral interactions is more appropriate for longer chains because of its built-in excluded volume interaction and the correct representation of 1−4 correlations. Summing up, both trimer and decamer potential sets can be used successfully to simulate 100- to 150-fold longer polymer molecules than those used for the fit.

These extrapolation factors are on the same order as found for poly(acrylic acid) in water[4] and considerably higher than most reported values for dilute polymer solutions and melts, e.g., polyisoprene (factor of approximately 12)[33] or PVA in hexane (factor of 6−15).[12] This could be due to our relatively "well-behaved" potentials; Reith[12] applied a more complicatedly shaped multiwell potential for PVA with many wells and maxima, which may amplify its state dependency.

Dynamics of Coarse-Grained versus Atomistic Simulations. The main advantage of coarse-graining is the direct (technical) speed-up (i.e., the CPU time we need for simulation of the same system in the coarse-grained vs atomistic representation), resulting mostly from smaller interaction site numbers and inexpensive calculations due to left-out electrostatics, and the indirect speed-up[7] in terms of faster sampling of configuration space. The latter results from flattening out of the system's potential surface. The molecules are less frequently trapped in local potential minima because interactions are softer and less

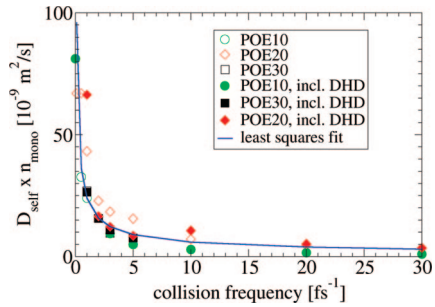

Figure 13. Dependence of the absolute diffusion coefficients in coarse-grained simulations on the Lowe−Andersen thermostat collision frequency (thermostat collision radius: 1 nm). We show a compilation of data $D_{self} \times n_{monomer}$ for POE_{10}, POE_{20}, and POE_{30} at w_{POE} = 0.48 and 298 K, comprising simulations using the decamer potentials with dihedrals (filled symbols) and without dihedrals (open symbols). The line shows a least-squares fit to the data.

far-ranging. As fast degrees of freedom have been removed, local rearrangement is also faster. To estimate this indirect speed-up, defined as $\alpha = t_{at}/t_{CG}$, we compare the long-time diffusion behavior at both levels of detail. Scaling the nominal time t_{CG} from CG simulations such that the resulting long-time diffusion behavior coincides with that of the atomistic simulation at time t_{at} gives an estimate of the speed-up factor α.

It has been shown for ideal model oligomers that the Lowe−Andersen thermostat influences the absolute value of diffusion coefficients, but it does not alter its dependence on chain length (the dynamical scaling).[34] We examined its influence on the diffusion for POE_{10} to POE_{30}, using the different decamer potentials. Figure 13 shows the compilation of these data for R_{th} = 1 nm and 298 K at constant polymer mass density (ρ_{POE} = 484 kg/m^3) over the collision frequency. Nearly all data fall on the same curve $D_{self}n_{mono}$ = const., which shows that the diffusion of mesoscopic oligomer chains follows the Rouse model, which is normally applied to unentangled polymer melts but not to solutions.[35] The influence of hydrodynamic interactions on the dynamics is thus not captured correctly by the coarse-grained model, where the solvent molecules are no longer present. On the other hand, the scaling of relaxation times as $\tau_{end} \sim N^{1.25, \ldots, 0.1.69}$ (compare Figure 9) is closer to Θ-solvent behavior than to melt behavior. The correct scaling of static properties (gyration radii, end-to-end distance) shows that the effect of solvent molecules on static properties is however captured correctly. The least-squares fit of diffusion coefficients (shown as a line in Figure 13) gives a power dependency on

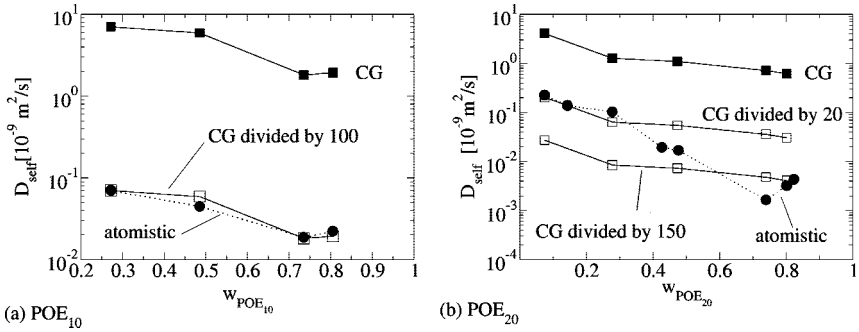

Figure 14. Self-diffusion coefficients of (a) POE10 and (b) POE_{20} at different concentrations as evaluated from atomistic (circles, designated "atomistic") and coarse-grained (filled squares, designated "CG") simulations (potential set without dihedrals; thermostat parameters: $R_{th} = 1$ nm and collision frequency 5 fs^{-1}). The additional curves with open symbols show the original CG diffusion coefficients divided by the indicated numbers to match the atomistic diffusion coefficient at lower or higher concentrations.

the collision frequency Γ as $D_{self}n_{mono} = 2.39\Gamma^{-0.6}$. The same strong dependency applies in turn for the speed-up. Hence, it is obvious that the dynamics of the CG simulations, differently from the static properties, depend very much on the thermostat parameters, whose influence is by far more important than the details of the potential. For small molecules, the thermostat influence may be smaller, as shown by Koopman and Lowe[29] for a dense LJ system; they found an only marginally reduced diffusion for low collision frequencies. This is most probably due to the larger thermostat radius we use here. For 5 collisions per femtosecond and $R_{th} = 1$ nm, we find approximate speed-up factors of 100 for the 10-mer, between 20 and 150 for the 20-mer, and approximately 25 for the 30-mer for the observed concentrations (compare Figure 14). For polymer melts, the authors of ref 23 found a unique speed-up of 53 for different chain lengths of 50−300 atoms for PE. They assumed that the same be valid for a POE melt, applying a coarsening level of 6 (our coarsening level is 3, i.e., three atomic sites in one CG site). However, the situation becomes less evident for simulations of polymer solutions. Here, the speed-up depends not only on chain length (and thermostat parameters in our case) but also on concentration. To exemplify the complex concentration dependency of diffusion in the CG simulations, we present in Figure 14 self-diffusion coefficients of POE_{10} and POE_{20} evaluated from atomistic and coarse-grained simulations (using the 10-mer potentials with dihedrals). CG diffusion coefficients are presented as evaluated from simulation (filled symbols) and after scaling with different indicated factors (open symbols), which were chosen to match CG and atomistic data either in the low or in the high concentration region. First, we note that, surprisingly, the concentration dependency is correctly captured for the decamer. A unique speed-up of approximately 100 applies at all examined concentrations for the applied thermostat parameters. For the 20-mer, this is only valid within the concentration region below $x = 0.018$ (which has the same monomer molar fraction as the potential fit). For higher concentrated systems, the speed-up factor increases, due to the stronger slowing of atomistic diffusion compared to the mesoscopic diffusion. The complex dependency on concentration of POE diffusion in atomistic simulations[21,22] originates not only from excluded volume interactions but also from solvent-specific interactions, which obviously cannot be represented in every (nonisotropic) detail within the implicit-solvent potential. The larger speed-up found for more dense systems may be an additional inherent advantage of the coarse-graining approach for POE if the focus is on static properties, as this extends the time scale in reach just within that region where it is needed the most. On the basis of our examinations, the speed-up must be determined separately for each concentration and thermostat parameter set if dynamic properties are to be derived from simulation, as the concentration dependency is not necessarily the same in atomistic and mesoscopic simulations. Evaluating the transferability of two sets of coarse-grained polymer potentials over temperature, Carbone et al. found that the speed-up decreased with increasing temperature, originating from different dependencies of diffusion on temperature on the atomistic and mesoscale.[19] They found comparable speed-ups as we did of 1−2 orders of magnitude. The same tendency was found by the authors of ref 20. Assuming that the lowest speed-up found (20 of the low-concentrated 20-mer) applies to longer chain lengths as well, the CG simulations we performed would refer to the physical time scale of some microseconds. Even longer times of some 10 μs would result from the speed-up factors observed for the 10-mer. The total speed-up in terms of CPU time per physical time unit is on the order of 1000, depending mainly on concentration and number of left-out interaction sites.

Summary

We evaluated in detail the transferability of coarse-grained potentials to both longer chain lengths and different concentrations. Three different sets of tabulated implicit-solvent coarse-grained potentials for POE in water were constructed using the iterative Boltzmann inversion technique in combination with coarse-grained molecular dynamics simulations. The target functions for the fit were extracted from atomistic simulations of (a) the trimer POE_3 ($H[CH_2-O-CH_2]_3H$) and (b) the decamer POE_{10} ($H[CH_2-O-CH_2]_{10}H$) in water at one intermediate concentration. The trimer was chosen, as it is the smallest analogue that incorporates all intramolecular interactions (except torsions) on the coarser level, and the decamer, as it better incorporates the chain character. Radii of gyration from coarse-grained simulations were compared to (a) extensive atomistic simulations of POE in TIP4P-Ew water and (b) experiments. Both potential sets could similarly well reproduce the atomistic radii of gyration (3−30 monomers) without explicit dihedral interactions. Experimental data for considerably greater molar masses of 150-fold larger poly(oxyethylene) chains than in the 10-mer fit (molecular mass 6.6×10^4 g/mol) could be reproduced semiquantitatively by the decamer potentials, simultaneously reproducing the correct scaling behavior. Its transferability could substantially be improved by the incorporation of a dihedral potential, which led to an almost quantitative reproduction of the experimental scaling law for R_G. The trimer potentials fitted to a dilute solution were applicable to higher

concentrations and to a lesser extent to more diluted solutions. Compared to the decamer potentials, the transferability of the trimer potentials seemed to be restricted to the range of 3−200 monomers. Simulations of larger molecules resulted in part in collapsed states, indicating a possible metastable behavior of the trimer potential. Thus, for the examined implicit-solvent POE models, the transfer of oligomer-fitted potentials to considerably (about 2 orders of magnitude) larger molecules is possible and yields almost quantitative structural agreement with experiments. The observation of chain collapse in some cases indicates, however, the existence of possible pitfalls. From comparisons of reorientations of end-to-end vectors and diffusion within the different models, we find a considerable acceleration using the coarse-grained potentials, which is however different for the different potential sets, all using the same coarse-graining level. The speed-up factor of D_{CG}/D_{at} is independent of concentration for the decamer simulated with optimized decamer-fitted potentials. It is dependent on concentration for all other considered chain lengths. The parameters of the Lowe−Andersen thermostat influence the absolute diffusion coefficients very much, but all oligomer simulations of 10−30 monomers at constant mass density show qualitatively the same behavior, with an ideal reciprocal dependency of diffusion coefficients on the number of monomers. Hence, the absolute speed-up is dependent on concentration, chain length, and thermostat parameters and ranges from 1−2 orders of magnitude.

Among the proposed potentials, the decamer-fitted set of potentials including dihedrals seems to be the most suitable for simulations of very large molecules as well as dense systems, since it performs best in reproducing atomistic and experimental structures, and it leads to the fastest decorrelation of end-to-end vectors among the assessed potentials. This set of potentials can be used to efficiently study structural or association *equilibrium* properties of large molecules built from POE units on the mesoscale. An important limit of our approach is that it cannot be used to study *dynamical* properties of large molecules quantitatively, due to the multifaceted dependencies of coarse-grained dynamics as explained above. Second, as our potentials are fitted to structure only, they cannot be expected to reproduce solution thermodynamics quantitatively. However, they can be used as very efficient means of speeding up the traveling through phase space to equilibrate and advance in time large atomistic structures. The mesoscale structures can be back-mapped[5,36,37] to the atomistic scale and then used for detailed atomistic simulations, or direct multiscale simulations[38] can be performed. Trajectories can then be evaluated for any thermodynamic or structural property of interest like solubility or interactions with specific substrates.

Acknowledgment. The authors are grateful to the *Deutsche Forschungsgemeinschaft* (SPP 1155) and to the Dortmund University of Technology for kindly providing computer time on its *Linux Cluster Dortmund* (LIDO). J.F. acknowledges valuable discussions with Prof. Müller-Plathe.

Supporting Information Available: The tabulated potentials for bonds, bends, and torsions are available in the form of two-column text files. The first column contains the coordinate, and the second column, the potential in units of kilojoules per mole. The bond-stretching potentials are tabulated in equidistant intervals of squared distances r^2 (nm^2), while angle and torsion potentials are tabulated in equidistant intervals of angles (rad). This material is available free of charge via the Internet at http://pubs.acs.org.

References and Notes

(1) Milano, G.; Goudeau, S.; Müller-Plathe, F. *J. Polym. Sci., Part B: Polym. Phys.* **2005**, *43*, 871.
(2) Baschnagel, J.; Binder, K.; Doruker, P.; Gusev, A. A.; Hahn, O.; Kremer, K.; Mattice, W. L.; Müller-Plathe, F.; Murat, M.; Paul, W.; Santos, S.; Suter, U. W.; Tries, V. *Adv. Polym. Sci.* **2000**, *152*, 41.
(3) Reith, D.; Meyer, H.; Müller-Plathe, F. *Macromolecules* **2001**, *34*, 2335.
(4) Reith, D.; Müller, B.; Müller-Plathe, F.; Wiegand, S. *J. Chem. Phys.* **2002**, *116*, 9100.
(5) Bedrov, D.; Ayyagari, C.; Smith, G. D. *J. Chem. Theory Comput.* **2006**, *2*, 598.
(6) Lyubartsev, A. P.; Laaksonen, A. *J. Chem. Phys.* **1999**, *111*, 11207.
(7) Depa, P. K.; Maranas, J. K. *J. Chem. Phys.* **2005**, 123.
(8) Henderson, R. L. *Phys. Lett. A* **1974**, *A 49*, 197.
(9) Jain, S.; Garde, S.; Kumar, S. K. *Ind. Eng. Chem. Res.* **2006**, *45*, 5614.
(10) Lyubartsev, A. P.; Laaksonen, A. *Phys. Rev. E* **1995**, *52*, 3730.
(11) Ashbaugh, H. S.; Patel, H. A.; Kumar, S. K.; Garde, S. *J. Chem. Phys.* **2005**, 122.
(12) Reith, D. Ph.D. thesis, Johannes Gutenberg-Universität Mainz, 2001.
(13) Reith, D.; Pütz, M.; Müller-Plathe, F. *J. Comput. Chem.* **2003**, *24*, 1624.
(14) Silbermann, J. R.; Klapp, S. H. L.; Schoen, M.; Chennamsetty, N.; Bock, H.; Gubbins, K. E. *J. Chem. Phys.* **2006**, *124*, 74105.
(15) Krakoviack, V.; Rotenberg, B.; Hansen, J. P. *J. Phys. Chem. B* **2004**, *108*, 6697.
(16) Hansen, J. P.; Addison, C. I.; Louis, A. A. *J. Phys.: Condens. Matter* **2005**, *17*, S3185.
(17) Izvekov, S.; Voth, G. A. *J. Chem. Phys.* **2005**, 123.
(18) Kamio, K.; Moorthi, K.; Theodorou, D. N. *Macromolecules* **2007**, *40*, 710.
(19) Carbone, P.; Varzaneh, H. A. K.; Chen, X. Y.; Muller-Plathe, F. *J. Chem. Phys.* **2008**, 128.
(20) Ghosh, J.; Faller, R. *Mol. Simul.* **2007**, *33*, 759.
(21) Fischer, J.; Paschek, D.; Geiger, A.; Sadowski, G. *J. Phys. Chem. B* **2008**, *112*, 2388.
(22) Fischer, J.; Paschek, D.; Geiger, A.; Sadowski, G. *J. Phys. Chem. B* **2008**, *112*, 8849.
(23) Chen, C. X.; Depa, P.; Sakai, V. G.; Maranas, J. K.; Lynn, J. W.; Peral, I.; Copley, J. R. D. *J. Chem. Phys.* **2006**, 124.
(24) Horn, H. W.; Swope, W. C.; Pitera, J. W.; Madura, J. D.; Dick, T. J.; Hura, G. L.; Head-Gordon, T. *J. Chem. Phys.* **2004**, *120*, 9665.
(25) Paschek, D.; Geiger, A. *Moscito 4*; Department of Physical Chemistry, University of Dortmund: Dortmund, Germany, 2002.
(26) Allen, M. P.; Tildesley, D. J. *Computer Simulations of Liquids*; Oxford Science Publications: Oxford, U.K., 1987.
(27) Lowe, C. P. *Europhys. Lett.* **1999**, *47*, 145.
(28) Andersen, H. C. *J. Chem. Phys.* **1980**, *72*, 2384.
(29) Koopman, E. A.; Lowe, C. P. *J. Chem. Phys.* **2006**, 124.
(30) Nikunen, P.; Karttunen, M.; Vattulainen, I. *Comput. Phys. Commun.* **2003**, *153*, 407.
(31) Vettorel, T.; Meyer, H. *J. Chem. Theory Comput.* **2006**, *2*, 616.
(32) Kawaguchi, S.; Imai, G.; Suzuki, J.; Miyahara, A.; Kitano, T. *Polymer* **1997**, *38*, 2885.
(33) Faller, R.; Reith, D. *Macromolecules* **2003**, *36*, 5406.
(34) Chen, L. J.; Lu, Z. Y.; Qian, H. J.; Li, Z. S.; Sun, C. C. *J. Chem. Phys.* **2005**, 122.
(35) Strobl, G. R. *The Physics of Polymers: Concepts for Understanding Their Structures and Behavior*; Springer: Berlin, Heidelberg, New York, 1996.
(36) Peter, C.; Delle Site, L.; Kremer, K. *Soft Matter* **2008**, *4*, 859.
(37) Harmandaris, V. A.; Adhikari, N. P.; van.der Vegt, N. F. A.; Kremer, K. *Macromolecules* **2006**, *39*, 6708.
(38) Praprotnik, M.; Delle Site, L.; Kremer, K. *Phys. Rev. E* **2006**, 73.
(39) Kinugasa, S.; Nakahara, H.; Fudagawa, N.; Koga, Y. *Macromolecules* **1994**, *27*, 6889.
(40) Devanand, K.; Selser, J. C. *Macromolecules* **1991**, *24*, 5943.

JP805770Q